Available online at www.sciencedirect.com

ScienceDirect

Geochimica et Cosmochimica Acta 334 (2022) 231–240

Geochimica et Cosmochimica Acta

www.elsevier.com/locate/gca

Mercury loss and isotope fractionation during high-pressure and high-temperature processing of sediments: Implication for the behaviors of mercury during metamorphism

Di Chen [a,b,1], Dongsheng Ren [c,1], Changzhou Deng [a], Zhendong Tian [a], Runsheng Yin [a,*]

[a] State Key Laboratory of Ore Deposit Geochemistry, Institute of Geochemistry, Chinese Academy of Scienceas, Guiyang 550081, China
[b] University of Chinese Academy of Sciences, Beijing 100049, China
[c] Institute of Geology, China Earthquake Administration, Beijing 100029, China

Received 3 May 2022; accepted in revised form 10 August 2022; available online 13 August 2022

Abstract

Metamorphic rocks show much lower mercury (Hg) levels than sedimentary rocks, which may be due to the loss of Hg during high-pressure and high-temperature conditions during metamorphism. To test this hypothesis, we conduct high-pressure and high-temperature experiments on ancient and modern sediments (WH black shale and GSS-4 soil). Under 0.3 GPa, the Hg concentrations decrease while the δ^{202}Hg values increase with rising temperatures (WH black shale: 333–89 ppb, −1.34 to −0.79‰, 250–700 °C; GSS-4: 545–265 ppb, −1.39 to −1.01‰, 400–700 °C), suggesting the loss of isotopically light Hg isotopes under high-temperature conditions. Under constant temperatures of both 200 °C and 500 °C, with increasing pressure (0.5–1.4 GPa), GSS-4 shows only a slight decrease in Hg concentration with no variation in δ^{202}Hg, suggesting that high-pressure conditions restrain the loss of isotopically lighter isotopes. Consistent Δ^{199}Hg and Δ^{200}Hg values were observed in both samples during our experiment, implying no Hg isotope mass-independent fractionation (Hg-MIF) under high-temperature and high-pressure conditions. While results of this imply that metamorphism may lead to the emission of isotopically lighter Hg from sedimentary rocks to the surface environment, the lack of Hg-MIF during metamorphism provides important support for the use of Hg isotopes for paleoenvironment reconstruction.

Keywords: Mercury; High-pressure and high-temperature; Metamorphism; Isotope fractionation

1. INTRODUCTION

Mercury (Hg) is a heavy metal of global concern for its active redox chemistry, strong bioaccumulation, long-range transport, and potent toxicity (Selin, 2009). As a result, the biogeochemical cycle of this metal in the surface systems (e.g., atmosphere, pedosphere, hydrosphere, biosphere) has been extensively studied (Selin, 2009). The deep cycle of Hg in the crust and mantle, via plate tectonics (Deng et al., 2021) and magmatism (Moynier et al., 2021; Yin et al., 2022), control the budget and the environmental impact of Hg in surface systems. Sedimentation, diagenesis, and metamorphism link the surface Hg cycle to the deep Hg cycle, however, the geochemical fate of Hg during these processes remains poorly constrained.

Past studies have reported similar Hg levels (mostly 10^2 to 10^3 parts per billion (ppb) by weight) in sediments and sedimentary rocks (Yin et al., 2015; Grasby et al., 2019;

* Corresponding author.
E-mail address: yinrunsheng@mail.gyig.ac.cn (R. Yin).
[1] These authors contributed equally.

https://doi.org/10.1016/j.gca.2022.08.010
0016-7037/

Shen et al., 2019a, 2020; Sun et al., 2022a), suggesting limited loss of Hg during sedimentation and diagenesis. Metamorphic rocks, however, commonly show much lower Hg levels (mostly < 10 ppb, Deng et al., 2022), implying a significant loss of Hg from sedimentary rocks during metamorphism. Hg is highly volatile and mobile under high-temperature and high-pressure conditions (Deng et al., 2022). Understanding the dynamics of Hg loss during metamorphism is critical, given that the lost Hg may continue to cycle into surface systems. As the degree of metamorphism is a function of pressures and temperatures (Baldwin et al., 2003), experimental works involving different pressure and temperature conditions are warranted to investigate the dynamics of Hg loss during metamorphism.

Mercury isotope geochemistry is an important tool to understand the geochemical cycle of Hg, as Hg can undergo both mass-dependent fractionation (MDF, expressed as δ^{202}Hg) and mass-independent fractionation (MIF, expressed as Δ^{199}Hg and expressed as Δ^{199}Hg) (Kwon et al., 2020). Hg-MDF occurs ubiquitously during various physical, chemical, and biological processes (Blum et al., 2014; Kwon et al., 2020). Kinetic processes under normal temperature and pressure conditions, such as photodegradation of MeHg and photoreduction of Hg(II) (Bergquist and Blum, 2007; Chandan et al., 2015), gaseous Hg(0) diffusion (Koster van Groos et al., 2014), microbial methylation and demethylation (Janssen et al., 2016) and volatilization of Hg(0) (Zheng et al., 2007), commonly result in the enrichment of lighter Hg isotopes (characterized by lower δ^{202}Hg values) in the product, leaving the residue with higher δ^{202}Hg values. Hg-MIF mainly occurs during specific photochemical reactions (Bergquist and Blum, 2007). Large variations of >10‰ in both δ^{202}Hg and Δ^{199}Hg have been observed in natural samples, which provide two-dimensional information on the sources (Yin et al., 2019a) and processes of Hg in the environment (Grasby et al., 2019).

A recent study by Deng et al. (2022) on metamorphic rocks inferred a significant loss of Hg, no systematic Hg-MDF and the absence of Hg-MIF during metamorphism; however, experimental work supporting these hypotheses remains lacking. To fill this knowledge gap, we conducted high-pressure and high-temperature experiments on ancient and modern sediments to investigate the dynamics of Hg loss and Hg isotope fractionation, and to gain insights into the behavior of Hg during metamorphism.

2. SAMPLES AND METHODS

2.1. High-pressure and high-temperature experiments

A black shale sample and a soil standard reference material (SRM), representing ancient and modern sediments, respectively, were selected in this study. The black shale sample (named WH) was collected from the Neoproterozoic Cryogenian Datangpo Formation, South China, and has a high TOC content (1.91 wt%) (Zhou et al., 2021). The soil SRM (GSS-4, yellow soil) was purchased and consisted mainly of clay minerals, with low TOC content (0.62 wt%). Prior to the experiment, the WH black shale sample was cleaned, air-dried, pulverized, and powdered to 200 mesh. The GSS-4 soil sample is a powdered SRM and therefore did not undergo additional processing.

High-pressure and high-temperature experiments on the two samples were performed on a DS 6 × 1400 t hinged-type Large Volume Press (LVP) at the Institute of Geochemistry, Chinese Academy of Sciences (IGCAS). The LVP has a large-capacity sample chamber (Ren et al., 2019), enabling loading of enough sample materials to further conduct Hg concentration and isotopic composition analyses. The LVP uses six independent pistons to extrude the cube pressure transmitting medium, resulting in a very wide high-pressure range (0–2.0 GPa). The anvils have a length of 44.5 mm (Ren et al., 2019). The specific experimental assembly is shown in Fig. 1. The external pressure transmission medium is pyrophyllite, and the internal pressure transmission medium is pyrophyllite and boron nitride. Pyrophyllite is calcined at 600 °C, and boron nitride is the sample tube. The graphite tube is used to heat the sample. The temperature of the sample is observed *in situ* by a thermocouple inserted into the center of the sample. The temperature gradient from the sample center to the thermocouple was <10 °C (Yin et al., 2019b), which ensures uniform heating of the sample. The hexagonal boron nitride tubes are very stable under high-pressure and high-temperature conditions and are not easy to react with other materials (Kostoglou et al., 2015). The hexagonal boron nitride exhibits a layered porous structure (Weng et al., 2016). The use of hexagonal boron nitride tubes fabricates a semi-open system (Yin et al., 2019b), allowing for Hg loss during heating.

Briefly, about 2.0 g of sample powder was pre-compressed and loaded into a hexagonal boron nitride tube and sealed on both ends with boron nitride discs. The hexagonal boron nitride tubes have a Hg blank of 5–10 ng, according to early analyses by a DMA80 direct Hg analyzer, much lower than that in the loaded samples (>700 ng and >1000 ng for WH and GSS-4, respectively; see Section 3). The hexagonal boron nitride tubes were placed into external pressure transmitting medium made of pyrophyllite in the LVP, and then experienced controlled pressures (0.3–1.4 GPa) and temperatures (50–700 °C). The LVP oil pressure boosting rate is 10 MPa/h, the heating rate is 20 °C/min, and the relationship between oil pressure and chamber pressure refers to the calibration curve of Ren et al. (2019). A stepped method was used to raise pressure and temperature to the target values, and the target pressures and temperatures were maintained for 18 h to ensure sufficient Hg loss from the samples. The experimental conditions are shown in Table 1. Before doing the experiments, we tested that the Hg concentrations of the samples remained consistent when the time was >12 h. The *in situ* pressure condition of some of the samples we studied is lower than 0.5 GPa. The experimental device of solid pressure transmission medium may have low accuracy in this pressure range, but our experimental assembly is credible through the detailed pressure calibration by Ren and Li (2022).

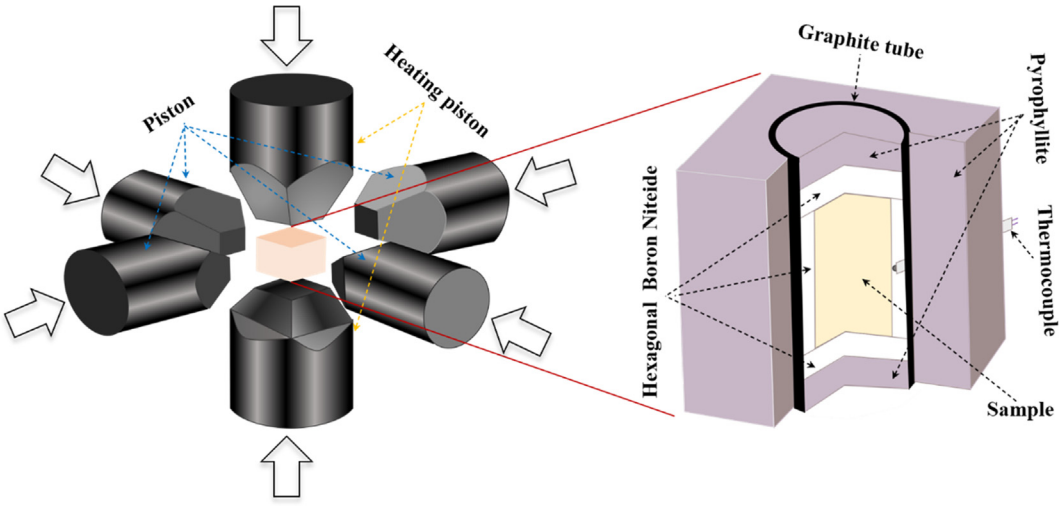

Fig. 1. Model diagram of experimental setup and sample chamber components (after Song et al., 2021).

Table 1
Sample information and specific experimental conditions during high-temperature and high-pressure experiments.

Sample ID	Rock type	Temperature (°C)	Pressure (GPa)	Time (hour)
WH-CS*	Black shale	20	/	/
WH-1	Black shale	100	0.3	18
WH-2	Black shale	150	0.3	18
WH-3	Black shale	200	0.3	18
WH-4	Black shale	250	0.3	18
WH-5	Black shale	300	0.3	18
WH-6	Black shale	400	0.3	18
WH-7	Black shale	450	0.3	18
WH-8	Black shale	500	0.3	18
WH-9	Black shale	700	0.3	18
GSS-4-CS*	Soil	20	/	/
GSS-4-1	Soil	50	0.3	18
GSS-4-2	Soil	100	0.3	18
GSS-4-3	Soil	300	0.3	18
GSS-4-4	Soil	400	0.3	18
GSS-4-5	Soil	500	0.3	18
GSS-4-6	Soil	600	0.3	18
GSS-4-7	Soil	200	0.5	18
GSS-4-8	Soil	200	0.8	18
GSS-4-9	Soil	200	1.1	18
GSS-4-10	Soil	200	1.4	18
GSS-4-11	Soil	500	0.5	18
GSS-4-12	Soil	500	0.8	18
GSS-4-13	Soil	500	1.1	18
GSS-4-14	Soil	500	1.4	18

* Experiments were during at standard atmospheric pressure and room temperature of 20 °C.

2.2. Hg concentration and isotopic composition analyses

After the experiments, the samples were powdered again into 200 mesh using an agate pestle and mortar for Hg concentration and isotopic composition analyses. Total Hg (THg) concentration and Hg isotopic composition of the samples were measured at the IGCAS.

Hg concentration was measured using a DMA-80 direct mercury analyzer (detection limit: 0.01 ng/g), which yielded Hg recoveries of 90 to 110% (n = 2) for the initial GSS-4 sample, which has a valid Hg concentration of 590 ± 50 ppb. Duplicate analysis of the initial WH black shale yielded uncertainty of <10% (2SD, n = 3).

A double-stage tube furnace coupled with 40% mixed acid (HNO_3/HCl = 2/1, *v*/*v*) trapping solutions was used for preconcentration of Hg from the samples for isotope analysis (Zerkle et al., 2020). The preconcentrated solutions were diluted to 0.5 ng/mL Hg in 10% acid and measured using a Neptune Plus multi-collector inductively coupled plasma mass spectrometer, following a previous method

(Yin et al., 2016). Hg-MDF is expressed in δ^{202}Hg notation in units of ‰ referenced to the NIST-3133 Hg standard (analyzed before and after each sample):

$$\delta^{202}\mathrm{Hg}(‰) = [(\mathrm{Hg}^{202}/^{198}\mathrm{Hg}_{\mathrm{sample}})/(\mathrm{Hg}^{202}/^{198}\mathrm{Hg}_{\mathrm{standard}}) - 1] \times 1000 \quad (1)$$

Hg-MIF is reported in Δ notation, which describes the difference between the measured δ^{xxx}Hg and the theoretically predicted δ^{xxx}Hg value, in units of ‰:

$$\Delta^{xxx}\mathrm{Hg} \approx \delta^{xxx}\mathrm{Hg} - \delta^{202}\mathrm{Hg} \times \beta \quad (2)$$

where β is 0.2520, 0.5024 and 0.7520 for Δ^{199}Hg, Δ^{200}Hg and Δ^{201}Hg, respectively (Bergquist and Blum, 2007). Duplicate or triplicate analyses for some of the samples were performed (Table 2). The NIST-3177 secondary standard solution was measured with the sample solutions. Our results of NIST-3177 (δ^{202}Hg: −0.58 ± 0.07‰, Δ^{199}Hg: −0.02 ± 0.05‰, Δ^{200}Hg: −0.01 ± 0.06‰, Δ^{201}Hg: −0.02 ± 0.05‰; 2SD, n = 8) and the initial GSS-4 soil SRM (δ^{202}Hg:-1.60 ± 0.07‰, Δ^{199}Hg:-0.48 ± 0.09‰, Δ^{200}Hg: −0.10 ± 0.05‰; Δ^{201}Hg:-0.41 ± 0.12‰; 2SD, n = 3) agrees well with previous studies (Bergquist and Blum, 2007; Zerkle et al., 2020; Deng, et al., 2021; Wang et al., 2021; Sun et al., 2022b).

3. RESULTS

The Hg concentrations and isotope composition are summarized in Table 2 and shown in Figs. 2–4. The mass loss of Hg from sedimentary rocks was small (<5%) during the experiment. In this regard, the concentration change of Hg can be used to reflect the mass loss of Hg during the experiments. Under the confining pressure of 0.3 GPa (Fig. 2a), the concentration change of Hg in the WH black shale is small (375–333 ppb) when the temperature is ≤250 °C, but quickly increases with rising temperature when the temperature is >250 °C (333–89 ppb). The concentration change of Hg in the GSS-4 soil was also small (563–545 ppb) when the temperature was ≤400 °C, but increases rapidly when the temperature is >400 °C (545–265 ppb) (Fig. 3a). When the temperature was consistent, i.e., under 200 °C and 500 °C (Fig. 4a), the concentration loss of Hg in the GSS-4 soil decreased with the increase of pressure (0.5–1.4 GPa).

Under a confining pressure of 0.3 GPa, the δ^{202}Hg values shifted positively with increase of temperature for both samples (Figs. 2b and 3b). For the WH black shale, the shift was small (0.27‰) when the temperature was ≤250 °C but increased dramatically (−1.34 to −0.79‰) when the temperature was >250 °C. For the GSS-4 soil, the shift was also small (−1.60 to −1.39‰) when the temperature was ≤400 °C, but increased from −1.39 to −1.01‰ when the temperature was >400 °C. When the temperature was consistent, i.e., under 200 °C and 500 °C (Fig. 4b), negative shifts of δ^{202}Hg with the increase of pressure (0.5–1.4 GPa) can be observed in the GSS-4 soil. Notably, the overall shift of δ^{202}Hg under 200 °C (0.04‰) was smaller than that under 500 °C (0.24‰).

During all the experiments, for both samples, the Δ^{199}Hg (Figs. 2c, 3c, and 4c) and Δ^{200}Hg (Figs. 2d, 3d, and 4d) values under different temperature or pressure conditions were consistent, taking the analytical uncertainties of Δ^{199}Hg (±0.05%, 2SD) and Δ^{200}Hg (±0.05%, 2SD) into account.

4. DISCUSSION

4.1. Loss of Hg during high-pressure and high-temperature processes

Mercury compounds are highly volatile and mobile, and can be released from rocks under high-temperature conditions (Smith et al., 2008; Meier et al., 2016; Sotiropoulou et al., 2019). In this study, under 0.3 GPa, the concentration of Hg from the WH black shale and GSS-4 soil decreased with rising temperature, implying temperature is an important factor leading to Hg loss during metamorphism. The small concentration change of Hg in the WH black shale when the temperature is ≤250 °C (375–333 ppb, Fig. 2a) and in GSS-4 soil when the temperature is ≤400 °C (563–545 ppb, Fig. 3a) suggests the releasing temperature is different in different types of samples. Hg exists in multiple phases in soil and sediments, including organic matter-bound, clay minerals-bond, and other phases (e.g., sulfides) (Ravichandran, 2004; Grasby et al., 2019; Shen et al., 2020). Different Hg phases in sedimentary rocks have different temperatures during mercury pyrolysis release (Reis et al., 2012; Rumayor et al., 2015). Organic-bound Hg has a low pyrolysis temperature of 200–300 °C, whereas clay-bound Hg has a pyrolysis temperature of 400–700 °C (Su et al., 2021). In this study, the concentration change of Hg in the WH black shale increases rapidly after 250 °C, which could be due to the release of organic matter-bound Hg, given that this sample is organic-rich (TOC: 1.91 wt%). A positive correlation ($p < 0.01$, $R = 0.89$) between Hg and TOC has been reported for the WH black shales (Zhou et al., 2021), suggesting Hg is mainly in an organic-bound form. The concentration change of Hg in GSS-4 soil is more significant when the temperature is >400 °C, suggesting clay mineral-bound Hg is the dominant Hg phase in this sample. Organic matter-bound Hg is minor in the GSS-4 soil, given its low TOC content (0.62 wt%).

Under consistent temperatures of both 200 °C and 500 °C, slightly lower Hg concentrations (493 ± 28–545 ± 13 pp b, Fig. 4a) were observed in GSS-4 soil at high pressures (0.5–1.4 GPa), compared to the accepted value for GSS-4 soil under normal temperature and pressure conditions (590 ± 50 ppb). Although THg analysis can yield uncertainty of up to 10%, the concentration loss of Hg in GSS-4 soil seems to decrease with rising pressure (Fig. 4a), implying that pressure is another important factor controlling the loss of Hg during metamorphism and more Hg tends to be lost under low-pressure conditions, consistent with the fact that volatilization potential is highest under low-pressure conditions (Huber et al., 2006).

Table 2
Hg concentration and Hg isotopic composition of the two studied samples under different temperature and pressure conditions.

Sample ID	THg (ppb)	δ^{199}Hg (‰)	SD	δ^{200}Hg (‰)	SD	δ^{201}Hg (‰)	SD	δ^{202}Hg (‰)	SD	Δ^{199}Hg (‰)	SD	Δ^{200}Hg (‰)	SD	Δ^{201}Hg (‰)	SD	N*
WH-CS	375	−0.22	0.02	−0.82	0.07	−1.13	0.07	−1.61	0.18	0.18	0.06	0.01	0.04	0.09	0.07	3
WH-1	359	−0.22	0.10	−0.67	0.07	−0.96	0.08	−1.41	0.04	0.14	0.09	0.04	0.05	0.09	0.05	2
WH-2	293	−0.23	0.03	−0.71	0.00	−1.01	0.04	−1.45	0.03	0.13	0.04	0.02	0.02	0.09	0.05	3
WH-3	334	−0.23		−0.65		−0.85		−1.42		0.13		0.06		0.21		1
WH-4	333	−0.18		−0.63		−0.90		−1.34		0.15		0.05		0.11		1
WH-5	281	−0.12	0.16	−0.55	0.16	−0.77	0.15	−1.18	0.16	0.18	0.12	0.04	0.08	0.12	0.03	2
WH-6	259	−0.11		−0.45		−0.61		−1.01		0.15		0.06		0.15		1
WH-7	187	−0.12	0.06	−0.56	0.07	−0.81	0.08	−1.15	0.15	0.17	0.02	0.02	0.01	0.05	0.04	2
WH-8	176	−0.02	0.07	−0.37	0.09	−0.52	0.09	−0.84	0.12	0.19	0.04	0.06	0.03	0.12	0.00	2
WH-9	89.1	−0.05	0.09	−0.35	0.08	−0.53	0.02	−0.79	0.06	0.15	0.07	0.04	0.05	0.06	0.03	2
GSS-4-CS	563	−0.89	0.04	−0.91	0.01	−1.61	0.05	−1.60	0.03	−0.48	0.05	−0.10	0.02	−0.41	0.06	3
GSS-4-1	546	−0.83		−0.75		−1.53		−1.48		−0.46		−0.01		−0.42		1
GSS-4-2	530	−0.82	0.09	−0.83	0.16	−1.53	0.14	−1.48	0.12	−0.44	0.06	−0.08	0.10	−0.42	0.05	2
GSS-4-3	541	−0.78		−0.76		−1.46		−1.46		−0.41		−0.03		−0.36		1
GSS-4-4	545	−0.83		−0.73		−1.40		−1.39		−0.48		−0.04		−0.36		1
GSS-4-5	377	−0.72	0.07	−0.66	0.11	−1.34	0.13	−1.28	0.10	−0.40	0.05	−0.02	0.06	−0.38	0.05	2
GSS-4-6	265	−0.68	0.04	−0.54	0.04	−1.14	0.05	−1.01	0.08	−0.42	0.02	−0.03	0.00	−0.38	0.01	2
GSS-4-7	526	−0.72		−0.66		−1.35		−1.28		−0.40		−0.01		−0.39		1
GSS-4-8	554	−0.71		−0.60		−1.34		−1.25		−0.39		0.03		−0.40		1
GSS-4-9	545	−0.76		−0.60		−1.42		−1.35		−0.41		−0.01		−0.40		1
GSS-4-10	555	−0.75		−0.68		−1.44		−1.32		−0.42		−0.02		−0.45		1
GSS-4-11	472	−0.71	0.03	−0.61	0.04	−1.29	0.09	−1.18	0.09	−0.41	0.05	−0.02	0.01	−0.41	0.02	2
GSS-4-12	467	−0.68		−0.54		−1.17		−1.07		−0.41		0.00		−0.37		1
GSS-4-13	511	−0.82		−0.76		−1.53		−1.47		−0.44		−0.02		−0.42		1
GSS-4-14	523	−0.77		−0.72		−1.48		−1.42		−0.42		0.00		−0.41		1

* Number of analysis, Hg isotope value is the average during this study.

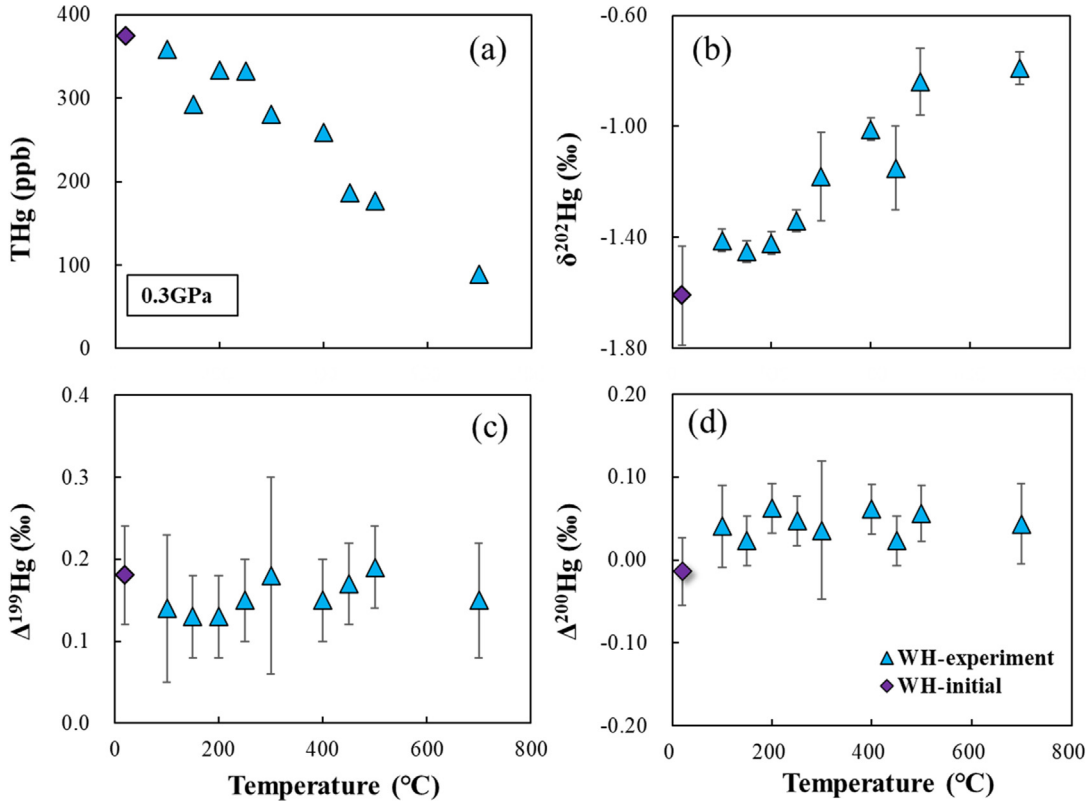

Fig. 2. (a) THg concentration vs temperature, (b) δ^{202}Hg vs temperature, (c) Δ^{199}Hg vs temperature, and (d) Δ^{200}Hg vs temperature diagrams for the WH black shale under 0.3 GPa. The mass loss of sedimentary rocks was small (<5%) during the experiment, therefore, the concentration loss of Hg can be used to reflect the mass loss of Hg during the experiments. The uncertainties displayed for δ^{202}Hg, Δ^{199}Hg and Δ^{200}Hg are the largest values of standard deviation (SD) for sample replicates, NIST-3177 and GSS-4. THg concentrations are reported as parts per billion (ppb) by weight.

4.2. Significant Hg-MDF during high-pressure and high-temperature processes

During our experiments, the δ^{202}Hg of the two investigated samples progressively change towards higher values with rising temperatures (Figs. 2b and 3b), indicating that light Hg isotopes are preferentially lost from the samples. The overall variations of δ^{202}Hg in our samples (WH: −1.61 to −0.79‰ and GSS-4 soil: −1.60 to −1.01‰) are relatively smaller than that observed during Hg biogeochemical processes under normal temperature and pressure conditions (0.5–3.0‰; Blum et al., 2014 and references therein), which is consistent with previous observations of other isotopes (e.g., Cd, Cu, Zn, Fe) that show small isotope fractionation during high-temperature processes (Hoefs and Hoefs, 1997). Interestingly, the δ^{202}Hg values of the WH black shale show limited change when the temperature is ≤250 °C, and change dramatically when the temperature is >250 °C (Fig. 2b). Similar characteristics can also be observed in the GSS-4 soil, but the turning point of temperature is ~400 °C (Fig. 3b). Previous research suggests that Hg in sediment can be associated with organic matter, sulfides, and clay minerals (Ravichandran, 2004; Grasby et al., 2019; Shen et al., 2020). Different Hg phases may have distinct Hg isotopic signatures (Yin et al., 2013a; Grigg et al., 2018), which may alternatively explain the temporal variation of δ^{202}Hg in the two studied samples. Nonetheless, we suggest that temperature can be an important factor in controlling the magnitude of Hg-MDF during Hg loss.

In contrast, it seems that the increase of pressure can restrain the loss of isotopically lighter isotopes, given that our samples show very small variations of δ^{202}Hg (200 °C: −1.28 to −1.32‰ and 500 °C: −1.18 to −1.42‰) under high-pressure conditions (0.5–1.4 GPa) when the temperatures were under both 200 °C and 500 °C (Fig. 4b).

4.3. No significant Hg-MIF during high-pressure and high-temperature processes

To date, only a few processes are found to trigger Hg-MIF. MIF of odd Hg isotopes (Δ^{199}Hg and Δ^{201}Hg) is explained by the nuclear volume effect (NVE) and magnetic isotope effect (MIE) (Blum et al., 2014). The Δ^{199}Hg/Δ^{201}Hg slope has been used to distinguish MIF due to NVE and MIE in natural samples (Kwon et al., 2020). MIF via NVE is characterized by Δ^{199}Hg/Δ^{201}Hg of 1.6–1.7 and is involved in the dark reduction of aqueous Hg(II) (Zheng and Hintelmann, 2010), Hg-thiol complexation (Wiederhold et al., 2010) and liquid Hg(0) evaporation (Estrade et al., 2009). MIF via MIE produces Δ^{199}Hg/Δ^{201}Hg of 1.0–1.3 and is commonly observed

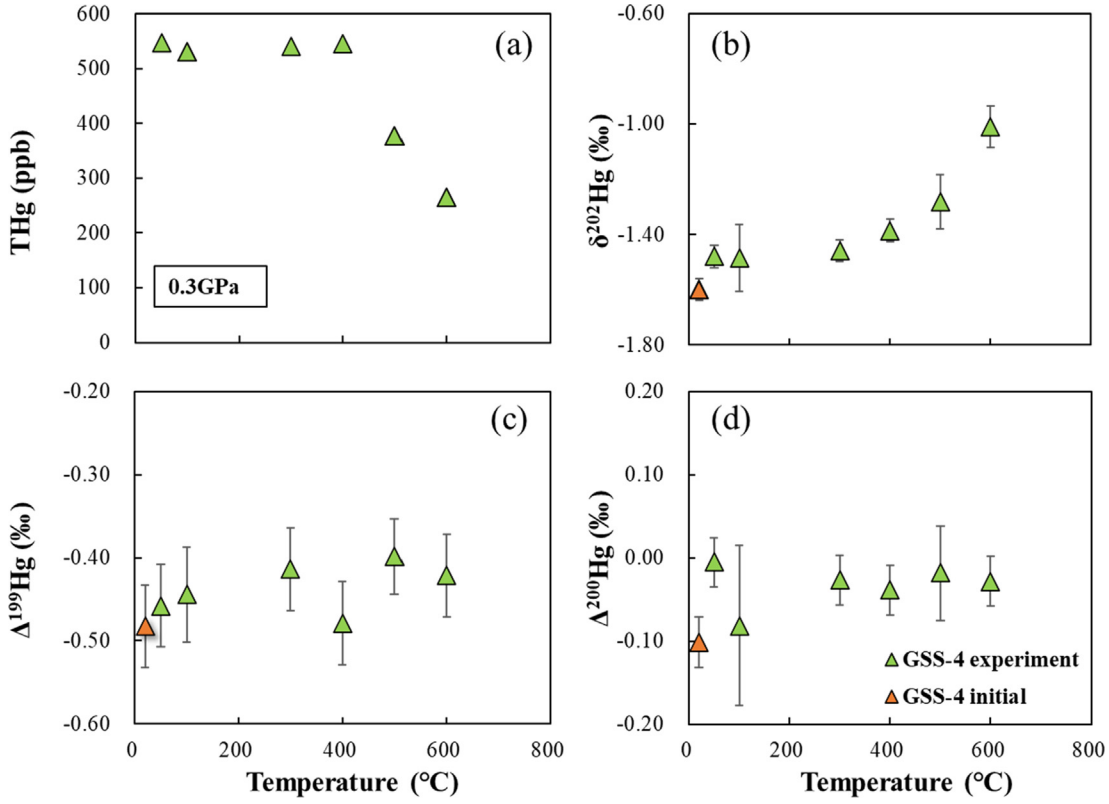

Fig. 3. (a) THg concentration vs temperature, (b) δ^{202}Hg vs temperature, (c) Δ^{199}Hg vs temperature, and (d) Δ^{200}Hg vs temperature diagrams for the GSS-4 soil under 0.3 GPa. The mass loss of sedimentary rocks was small (<5%) during the experiment, therefore, the concentration loss of Hg can be used to reflect the mass loss of Hg during the experiments. The uncertainties displayed for δ^{202}Hg, Δ^{199}Hg and Δ^{200}Hg are the largest values of standard deviation (SD) for sample replicates, NIST-3177 and GSS-4.

during aqueous Hg(II) photoreduction and MeHg photodegradation (Bergquist and Blum, 2007; Zheng and Hintelmann, 2009; Kwon et al., 2020). The mechanism of MIF of even isotopes (Δ^{200}Hg) remains unclear, however, it is thought to relate to photo-oxidation of gaseous Hg (0) (Sun et al., 2016).

Our experiments were conducted in the absence of light and yielded consistent Δ^{199}Hg and Δ^{200}Hg values for both samples under different temperature and pressure conditions (Figs. 2c, d, 3c, d, 4c, and d), suggesting the lack of MIF for both odd and even Hg isotopes during the high-pressure and high-temperature processes. The Δ^{199}Hg/Δ^{201}Hg ratio of ~1 for the studied samples under different temperature and pressure conditions (Fig. 5) is consistent with that observed in natural samples (reviewed by Blum et al., 2014), which again confirms no Hg-MIF during the experiment. The results of this study agree well with a recent study by Deng et al. (2022), which reported similar Δ^{199}Hg values in metamorphic rocks and their parent sedimentary rocks and hypothesized no Hg-MIF during metamorphism. The positive Δ^{199}Hg values of the WH black shale agree well with that observed in marine sediments (Yin et al., 2015, 2017), suggesting that Hg was sourced from seawater. The negative Δ^{199}Hg values of the GSS-4 soil agree well with previous results on soil and vegetation (Biswas et al., 2008; Demers et al., 2013; Yin et al., 2013b), suggesting that Hg originated from atmospheric Hg(0) deposition.

5. CONCLUSIONS AND IMPLICATIONS FOR HG GEOCHEMICAL CYCLE AND PETROGENETIC TRACING

Our results show that under high-temperature metamorphic conditions, lighter Hg isotopes are preferentially lost from sediments, but the increase of pressure seems to restrain the loss of isotopically lighter isotopes. Although we caution that our experiments may not fully represent slowly occurring metamorphic processes, our results can provide insights into the behavior of Hg during metamorphism. Various forms of metamorphism such as regional and contact metamorphism, involving high-pressure and high-temperature processing of sedimentary rocks, may induce loss of isotopically lighter Hg from the metamorphosed sediments, leading to Hg migration in the crust and resulting in lower Hg contents and higher δ^{202}Hg values in metamorphic basement rocks (Deng et al., 2022). These results suggest that metamorphism could be an important part of the Hg geochemical cycle, as the lost Hg would either directly return to the surface systems as gaseous Hg(0) form, increasing its lifetime to cycle in the environment, or be involved in the metallogenesis of economically important Hg-rich ore deposits as soluble Hg(II) form. In the future, investigation of the loss pathways of Hg (in gaseous or soluble forms), based on experimental approaches or field observation, is warranted

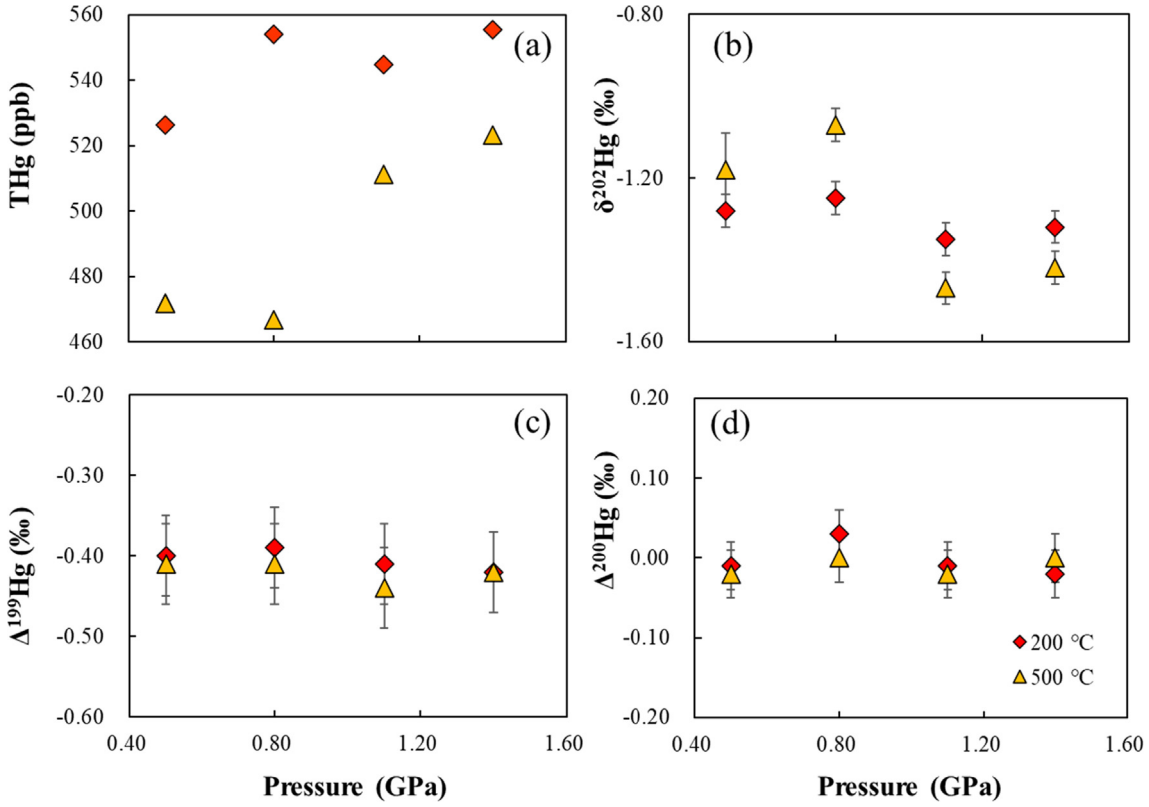

Fig. 4. (a) THg concentration vs pressure, (b) δ^{202}Hg vs pressure, (c) Δ^{199}Hg vs pressure, and (d) Δ^{200}Hg vs pressure diagrams for the GSS-4 soil under 200 °C and 500 °C. The mass loss of sedimentary rocks was small (<5%) during the experiment, therefore, the concentration loss of Hg can be used to reflect the mass loss of Hg during the experiments. The uncertainties displayed for δ^{202}Hg, Δ^{199}Hg and Δ^{200}Hg are the largest values of standard deviation (SD) for sample replicates, NIST-3177 and GSS-4.

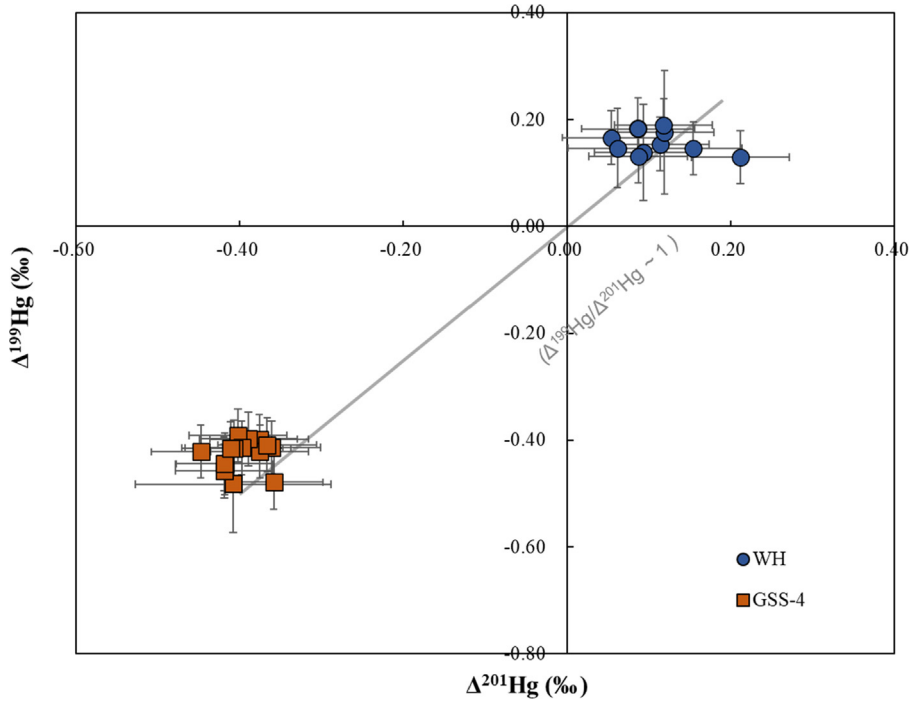

Fig. 5. Δ^{199}Hg versus Δ^{201}Hg diagram for WH black shale and GSS-4 soil samples.

to fully access the ultimate fate of the Hg lost during metamorphism.

Growing studies have used Hg concentrations and isotopic composition in sediments to understand the paleoenvironment, revealing key events in Earth's history such as large igneous provinces eruption, mass extinction, and oceanic redox changes (Sanei et al, 2012; Grasby et al., 2013, 2019; Shen et al., 2019a, 2019b,2022; Zerkle et al., 2020). Our study makes an important contribution by showing that there is very little Hg lost or isotope fractionation at normal temperatures during burial and diagenesis processes. This speaks to the fidelity of the sedimentary record of Hg and points to the reliability of the records. However, metamorphism involving high-temperature and high-pressure processing may lead to changes in Hg concentrations and δ^{202}Hg values, so caution is required when using these proxies for paleoenvironment reconstruction when dealing with metamorphosed rocks. Fortunately, Hg-MIF signals (Δ^{199}Hg, Δ^{200}Hg, and Δ^{201}Hg) may still be a useful proxy, given that no Hg-MIF occurs during metamorphic processes. As such, our study may provide important support for the use of Hg isotopes for paleoenvironment reconstruction, although more studies should be conducted to fully consider the diversity of samples.

DATA AVAILABILITY

Data will be made available on request.

DECLARATION OF COMPETING INTEREST

The authors declare that they have no known competing financial interests or personal relationships that could have appeared to influence the work reported in this paper.

ACKNOWLEDGEMENTS

This work was supported by the Natural Science Foundation of China (41873047).

APPENDIX A. SUPPLEMENTARY MATERIAL

Supplementary material to this article can be found online at https://doi.org/10.1016/j.gca.2022.08.010.

REFERENCES

Baldwin J., Bowring S. and Williams M. (2003) Petrological and geochronological constraints on high pressure, high temperature metamorphism in the Snowbird tectonic zone, Canada. *J. Metamorph. Geol.* **21**, 81–98.

Bergquist B. A. and Blum J. D. (2007) Mass-dependent and -independent fractionation of Hg isotopes by photoreduction in aquatic systems. *Science* **318**, 417–420.

Biswas A., Blum J. D., Bergquist B. A., Keeler G. J. and Xie Z. (2008) Natural mercury isotope variation in coal deposits and organic soils. *Environ. Sci. Technol.* **42**, 8303–8309.

Blum J. D., Sherman L. S. and Johnson M. W. (2014) Mercury isotopes in Earth and environmental sciences. *Annu. Rev. Earth Planet. Sci.* **42**(1), 249–269.

Chandan P., Ghosh S. and Bergquist B. A. (2015) Mercury isotope fractionation during aqueous photoreduction of monomethylmercury in the pcresence of dissolved organic matter. *Environ. Sci. Technol.* **49**, 259–267.

Demers J. D., Blum J. D. and Zak D. R. (2013) Mercury isotopes in a forested ecosystem: implications for air-surface exchange dynamics and the global mercury cycle. *Global. Biogeochem. Cy.* **27**, 222–238.

Deng C., Sun G., Rong Y., Sun R., Sun D., Lehmann B. and Yin R. (2021) Recycling of mercury from the atmosphere-ocean system into volcanic-arc–associated epithermal gold systems. *Geology* **49**, 309–313.

Deng C., Geng H., Xiao T., Chen D., Sun G. and Yin R. (2022) Mercury isotopic compositions of the Precambrian rocks and implications for tracing mercury cycling in Earth's interior. *Precambri. Res.* **373**, 106646.

Estrade N., Carignan J., Sonke J. E. and Donard O. F. X. (2009) Mercury isotope fractionation during liquid–vapor evaporation experiments. *Geochim. Cosmochim. Acta* **73**, 2693–2711.

Grasby S. E., Sanei H., Beauchamp B. and Chen Z. (2013) Mercury deposition through the Permo-Triassic Biotic Crisis. *Chem. Geol.* **351**, 209–216.

Grasby S. E., Them T. R., Chen Z. H., Yin R. S. and Ardakani O. H. (2019) Mercury as a proxy for volcanic emissions in the geologic record. *Earth Sci. Rev.* **196**, 102880.

Grigg A. R., Kretzschmar R., Gilli R. S. and Wiederhold J. G. (2018) Mercury isotope signatures of digests and sequential extracts from industrially contaminated soils and sediments. *Sci. Total Environ.* **636**, 1344–1354.

Hoefs J. and Hoefs J. (1997) *Stable Isotope Geochemistry*. Springer-Verlag, Berlin, pp. 142–177.

Huber M. L., Laesecke A. and Friend D. G. (2006) Correlation for the vapor pressure of mercury. *Ind. Eng. Chem. Res.* **45**(21), 7351–7361.

Janssen S. E., Schaefer J. K., Barkay T. and Reinfelder J. R. (2016) Fractionation of mercury stable isotopes during microbial methylmercury production by iron- and sulfate-reducing bacteria. *Environ. Sci. Technol.* **50**, 8077–8083.

Koster van Groos P. G., Esser B. K., Williams R. W. and Hunt J. R. (2014) Isotope effect of mercury diffusion in air. *Environ. Sci. Technol.* **48**, 227–233.

Kostoglou N., Polychronopoulou K. and Rebholz C. (2015) Thermal and chemical stability of hexagonal boron nitride (h-BN) nanoplatelets. *Vacuum* **112**, 42–45.

Kwon S. Y., Blum J. D., Yin R., Tsui M.-T.-K., Yang Y. H. and Choi J. W. (2020) Mercury stable isotopes for monitoring the effectiveness of the Minamata convention on mercury. *Earth Sci. Rev.* **203**, 103111.

Meier M. M. M., Cloquet C. and Marty B. (2016) Mercury (Hg) in meteorites: variations in abundance, thermal release profile, mass-dependent and mass-independent isotopic fractionation. *Geochim. Cosmochim. Acta* **182**, 55–72.

Moynier F., Jackson M. G., Zhang K., Cai H., Halldórsson S. A., Pik R., Day J. M. D. and Chen J. (2021) The mercury isotopic composition of Earth's mantle and the use of mass independently fractionated Hg to test for recycled crust. *Geophys. Res. Lett.* **48**(17), e2021GL094301.

Ravichandran M. (2004) Interactions between mercury and dissolved organic matter–a review. *Chemosphere* **55**, 319–331.

Reis A. T., Coelho J. P., Rodrigues S. M., Rocha R., Davidson C. M., Duarte A. C. and Pereira E. (2012) Development and validation of a simple thermo-desorption technique for mercury speciation in soils and sediments. *Talanta* **99**, 363–368.

Ren D. and Li H. (2022) Pressure calibration of large-volume press: a case study of hinged 6–8 type large-volume high-pressure apparatus. *Front. Earth. Sci.* **10**(10), 851813.

Ren D., Li H. and Shan S. (2019) The application of manganin wire pressure gauges in a large volume press under high-temperature conditions. *High Pressure Res* **39**, 619–627.

Rumayor M., Diaz-Somoano M., Lopez-Anton M. A. and Martinez-Tarazona M. R. (2015) Application of thermal desorption for the identification of mercury species in solids derived from coal utilization. *Chemosphere* **119**, 459–465.

Sanei H., Grasby S. E. and Beauchamp B. (2012) Latest Permian mercury anomalies. *Geology* **40**, 63–66.

Selin N. E. (2009) Global biogeochemical cycling of mercury: a review. *Annu. Rev. Environ. Resour.* **34**, 43–63.

Shen J., Algeo T. J., Chen J., Planavsky N. J., Feng Q., Yu J. and Liu J. (2019a) Mercury in marine Ordovician/Silurian boundary sections of South China is sulfide-hosted and non-volcanic in origin. *Earth Planet. Sci. Lett.* **511**, 130–140.

Shen J., Algeo T. J., Planavsky N. J., Yu J., Feng Q., Song H., Song H., Rowe H., Zhou L. and Chen J. (2019b) Mercury enrichments provide evidence of Early Triassic volcanism following the end-Permian mass extinction. *Earth Sci. Rev.* **195**, 191–212.

Shen J., Feng Q., Algeo T. J., Liu J., Zhou C., Wei W., Liu J., Them T. R., Gill B. C. and Chen J. (2020) Sedimentary host phases of mercury (Hg) and implications for use of Hg as a volcanic proxy. *Earth Planet. Sci. Lett.* **543**, 116333.

Shen J., Yin R., Algeo T. J., Svensen H. H. and Schoepfer S. D. (2022) Mercury evidence for combustion of organic-rich sediments during the end-Triassic crisis. *Nat. Commun.* **13**, 1–8.

Smith C. N., Kesler S. E., Blum J. D. and Rytuba J. J. (2008) Isotope geochemistry of mercury in source rocks, mineral deposits and spring deposits of the California Coast Ranges, USA. *Earth Planet. Sci. Lett.* **269**, 399–407.

Song G., Ma D., Zhou X., Wang L., Wei Z., Xu C., Wang W., Wang L., Zhao Y. and Wang S. (2021) Operation of large-volume cubic press above 8 GPa and 2500°C with a centimeter-sized cell volume using an optimized hybrid assembly. *High Pressure Research* **41**, 132–141.

Sotiropoulou R. E. P., Serafidou M. and Skodras G. (2019) Thermal mercury removal from coals: effect of pyrolysis conditions and kinetic analysis. *Fuel* **238**, 44–50.

Su Y., Liu X., Teng Y. and Zhang K. (2021) Mercury speciation in various coals based on sequential chemical extraction and thermal analysis methods. *Energies* **14**(9), 2361.

Sun R., Yao H., Deng C., Grasby S. E., Wang C., Chen X. and Yin R. (2022b) Volcanism-triggered climatic control on Late Cretaceous oceans. *Geochem. Geophys. Geosyst.* **23**, e2021GC010292.

Sun R., Grasby S. E., Shen J., Xiao J. and Yin R. (2022a) Climate/ocean dynamics and possible atmospheric mercury depletion events during the Late Sturtian deglaciation. *Chem. Geol.*, 120830.

Sun G., Sommar J., Feng X., Lin C.-J., Ge M., Wang W., Yin R., Fu X. and Shang L. (2016) Mass-dependent and -independent fractionation of mercury isotope during gas-phase oxidation of elemental mercury vapor by atomic Cl and Br. *Environ. Sci. Technol.* **50**, 9232–9241.

Wang X., Deng C., Yang Z., Zhu J.-J. and Yin R. (2021) Oceanic mercury recycled into the mantle: evidence from positive Δ^{199}Hg in lamprophyres. *Chem. Geol.* **584**, 120505.

Weng Q., Wang X., Wang X., Bando Y. and Golberg D. (2016) Functionalized hexagonal boron nitride nanomaterials: emerging properties and applications. *Chem. Soc. Rev.* **45**, 3989–4012.

Wiederhold J. G., Cramer C. J., Daniel K., Infante I., Bourdon B. and Kretzschmar R. (2010) Equilibrium mercury isotope fractionation between dissolved Hg(II) species and thiol-bound Hg. *Environ. Sci. Technol.* **44**, 4191–4197.

Yin R., Feng X., Wang J., Bao Z., Yu B. and Chen J. (2013a) Mercury isotope variations between bioavailable mercury fractions and total mercury in mercury contaminated soil in Wanshan mercury mine, SW China. *Chem. Geol.* **336**, 80–86.

Yin R., Feng X. and Meng B. (2013b) Stable mercury isotope variation in rice plants (Oryza sativa L.) from the Wanshan mercury mining district, SW China. *Environ. Sci. Technol.* **47**, 2238–2245.

Yin R., Feng X., Chen B., Zhang J., Wang W. and Li X. (2015) Identifying the sources and processes of mercury in subtropical estuarine and ocean sediments using Hg isotopic composition. *Environ. Sci. Technol.* **49**, 1347–1355.

Yin R., Krabbenhoft D. P., Bergquist B. A., Zheng W., Lepak R. F. and Hurley J. P. (2016) Effects of mercury and thallium concentrations on high precision determination of mercury isotopic composition by Neptune Plus multiple collector inductively coupled plasma mass spectrometry. *J. Anal. At. Spectrom.* **31**, 2060–2068.

Yin R., Xu L., Lehmann B., Lepak R. F., Hurley J. P., Mao J., Feng X. and Hu R. (2017) Anomalous mercury enrichment in early Cambrian black shales of South China: mercury isotopes indicate a seawater source. *Chem. Geol.* **467**, 159–167.

Yin R., Deng C., Lehmann B., Sun G., Lepak R. F., Hurley J. P., Zhao C., Xu G., Tan Q., Xie Z. and Hu R. (2019a) Magmatic-hydrothermal origin of mercury in Carlin-style and epithermal Gold deposits in China: evidence from mercury stable isotopes. *ACS Earth Space Chem.* **3**, 1631–1639.

Yin R., Chen D., Pan X., Deng C., Chen L., Song X., Yu S., Zhu C., Wei X., Xu Y., Feng X., Blum J. D. and Lehmann B. (2022) Mantle Hg isotopic heterogeneity and evidence of oceanic Hg recycling into the mantle. *Nat. Commun.* **13**(1), 1–7.

Yin Y., Li Z. and Zhai S. (2019b) The phase diagram of the Fe-P binary system at 3 GPa and implications for phosphorus in the lunar core. *Geochim. Cosmochim. Acta* **254**, 54–66.

Zerkle A. L., Yin R., Chen C., Li X., Izon G. J. and Grasby S. E. (2020) Anomalous fractionation of mercury isotopes in the Late Archean atmosphere. *Nat Commun* **11**, 1709.

Zheng W., Foucher D. and Hintelmann H. (2007) Mercury isotope fractionation during volatilization of Hg(0) from solution into the gas phase. *J. Anal. At. Spectrom.* **22**, 1097–1104.

Zheng W. and Hintelmann H. (2009) Mercury isotope fractionation during photoreduction in natural water is controlled by its Hg/DOC ratio. *Geochim. Cosmochim. Acta* **73**, 6704–6715.

Zheng W. and Hintelmann H. (2010) Nuclear field shift effect in isotope fractionation of mercury during abiotic reduction in the absence of light. *J. Phys. Chem. A* **114**, 4238–4245.

Zhou T., Pan X., Sun R., Deng C., Shen J., Kwon S. Y., Grasby S. E., Xiao J. and Yin R. (2021) Cryogenian interglacial greenhouse driven by enhanced volcanism: evidence from mercury records. *Earth Planet. Sci. Lett.* **564**, 116902.

Associate editor: Eva Stueeken